

Measurements of beam characteristics relevant  
to DUV MICROLITHOGRAPHY on a KrF EXCIMER LASER

Richard Sandstrom

Cymer Laser Technologies  
7887 Dunbrook Road, San Diego, CA 92126

**ABSTRACT**

We present measurements of several optical characteristics of the 248 nm beam produced by a spectrally narrowed KrF excimer laser designed for the deep ultraviolet reduction stepper. These measurements include intensity, divergence, and polarization profiles, spectral content, and coherence properties. Using a special high resolution spectrometer, we have established an upper limit of 2.27 pm FWHM for the spectral bandwidth, in agreement with measurements made with a diagnostic etalon. We have also found that the wavelength varies across the horizontal profile of the beam at a linear rate of 0.59 pm/mm. No comparable wavelength variation is seen in the vertical direction. Coherence measurements show that the vertical and horizontal spatial coherence lengths are different, 60 mm and 126 mm respectively. The temporal coherence length is 33.3 mm, in good agreement with the measured bandwidth.

**1. INTRODUCTION**

Deep ultraviolet microlithography is advancing rapidly, in part due to the development of high performance, spectrally narrowed excimer lasers for use as DUV sources. In order to integrate these laser sources into photolithographic equipment, and to properly model and improve the imaging process, optical designers require a detailed knowledge of the beam characteristics. In this paper we investigate the optical characteristics of the beam produced by a spectrally narrowed excimer laser (Cymer's model CX-2LS). This laser has been developed specifically for use as a DUV source for the next generation of photolithographic reduction steppers.

The design and overall performance details of the CX-2LS have been previously presented (Ref. 1). In brief, the CX-2LS is a KrF excimer laser which produces 3 watts of average power at 248 nm at a pulse repetition rate of 200 Hz. A grating-based line narrowing arrangement reduces the bandwidth to less than 3 pm, and allows the central wavelength to be tuned to anywhere in the wavelength range 248.0-248.6 nm. A highly stable wavemeter measures and maintains the output wavelength to within  $\pm 0.5$  pm.

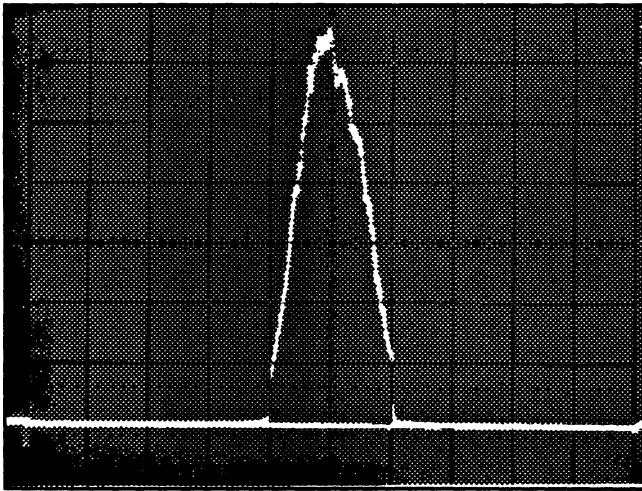
The data presented here include measurements of intensity and divergence profiles, polarization, spectral content, and coherence properties. Except as noted, all measurements were taken in a plane 1 meter from the

output aperture of the laser, with the laser operating at 200 Hz, producing 3 W of average power.

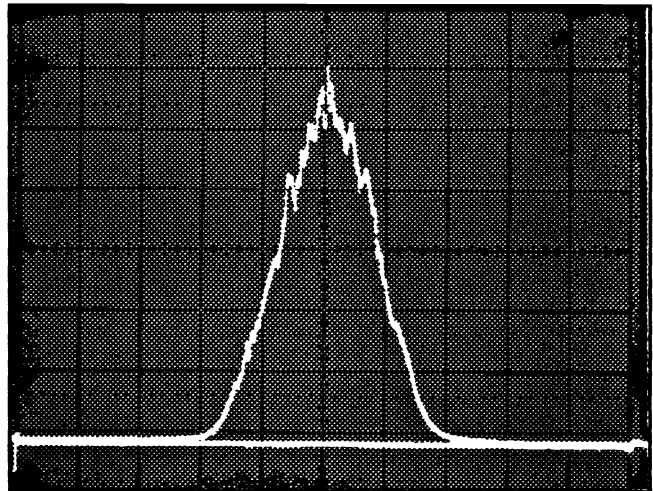
**2. BEAM PROFILE**

Profiles of the beam were obtained using a 1024 element linear photodiode array, providing cross-sectional slices of the rectangular (approximately 4 mm wide by 17 mm tall) intensity distribution. The data from the photodiode array could be scanned out quickly enough to give a profile scan for every pulse with the laser operating at 200 Hz. Care was taken to attenuate the beam to the level required by the photodiode array cleanly, without introducing artifacts. One arrangement which works well is to take three successive reflections off of uncoated, wedged fused silica substrates at near normal incidence. The latter consideration is important for preserving the polarization state of the beam - a substrate inclined at 45° to the beam, for instance, will preferentially reflect the s-polarization component over 10 times better than the p component. Unless the beam were randomly polarized, which will be shown not to be the case here, this would lead to a distorted measurement of the true profile.

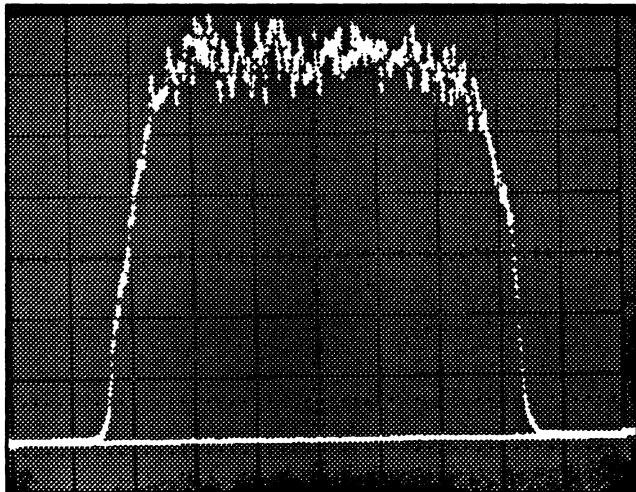
Measurements of the beam profile were first taken using a 50 cm lens to perform 1:1 imaging of the plane of the output coupler (the partially reflective mirror on the output end of the laser resonator) onto the photodiode array. Figures 1(a) and 1(b) each represent a



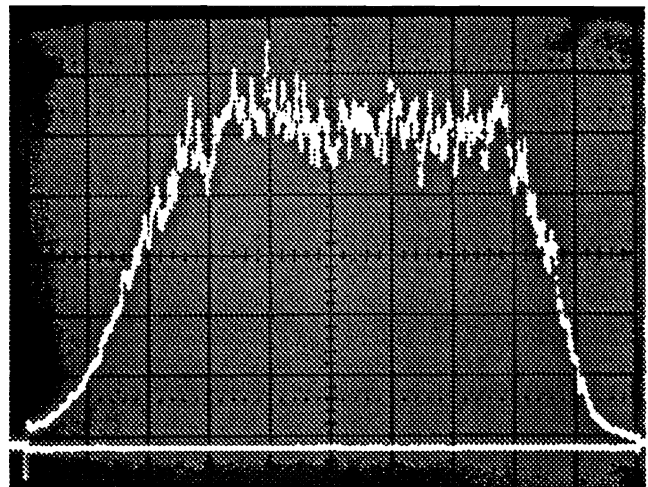
1(a)



2(a)



1(b)



2(b)

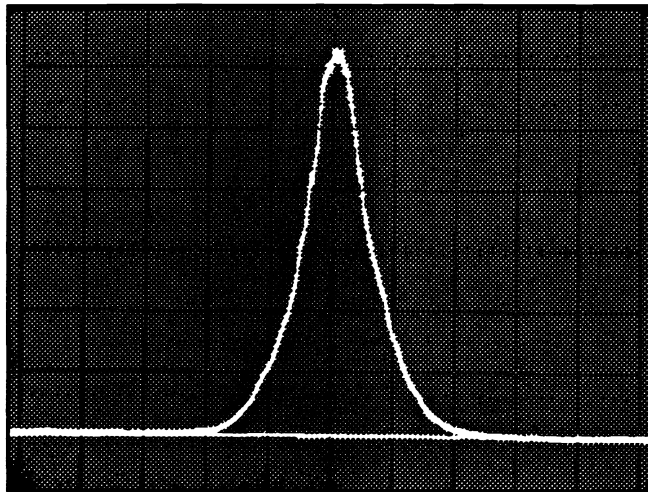
*Figure 1(a)(b) Horizontal (a) and vertical (b) intensity profiles taken by imaging the plane of the output coupler and aperture. Horizontal scale 2.5 mm/div.*

single pulse taken during 200 Hz, 3 W operation of the laser. Figure (a) is the horizontal profile taken through beam center, showing a 3.4 mm FWHM width. The profile is approximately Gaussian, except for some clipping of the skirts by a 5 mm aperture located in front of the output coupler. Figure (b) is a vertical slice through beam center, showing the vertical profile to be a fairly square top-hat, and 16 mm wide FWHM. The aspect ratio of the beam is set primarily by the dimensions of the discharge, and by the internal apertures within the resonator optics.

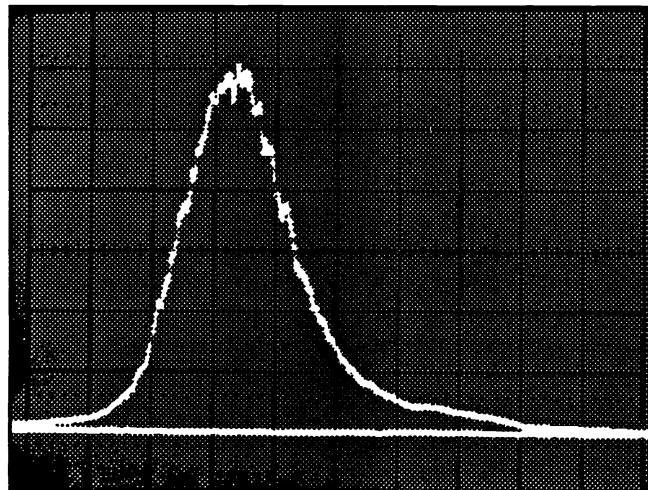
Next, the 50 cm lens was removed, the photodiode

*Figure 2 (a) (b). Horizontal (a) and vertical (b) intensity profiles taken through beam center, 1 meter away from the laser. Horizontal scale 2.5 mm/div.*

array repositioned, and the beam profile measured at a distance of 1 meter away from the laser. Beam divergence can be seen to have broadened the horizontal profile at 1 meter, shown in Figure 2(a), to 4.4 mm FWHM. Divergence effects have also softened the abrupt clipping in the skirts, to the point where the effects of the 5mm aperture are no longer discernable. The vertical profile at 1 meter, Figure 2(b), has become wider also, with a FWHM width of 17.7 mm. An asymmetry has crept into the profile, implying that the vertical beam divergence (to be measured in the next section) is asymmetric also.



3(a)



3(b)

Figure 3 (a) (b). Horizontal (a) and vertical (b) divergence profiles, single trace at 200 Hz. Horizontal scale 1 mR/div.

### 3. BEAM DIVERGENCE

Beam divergence and pointing stability were measured by Fourier transformation of the beam with a lens. The optical arrangement utilized the same attenuation scheme employed for the beam profile measurements. After attenuation, the beam passed through a 1 meter focal length lens and was brought to a focus onto the photodiode array. The array was mounted on a rotary holder, allowing it to be oriented to scan through the focus in either a horizontal or vertical direction, thereby measuring the horizontal or vertical divergence profiles. The relation between the angular spectrum

and the distance from center in the focal (Fourier) plane is (for small angles)  $\theta = r/f$ , where  $r$  is the radial distance from center, and  $f$  is the focal length of the lens. By using appropriate scale factors, the scan of the photodiode array may be directly calibrated in angular units.

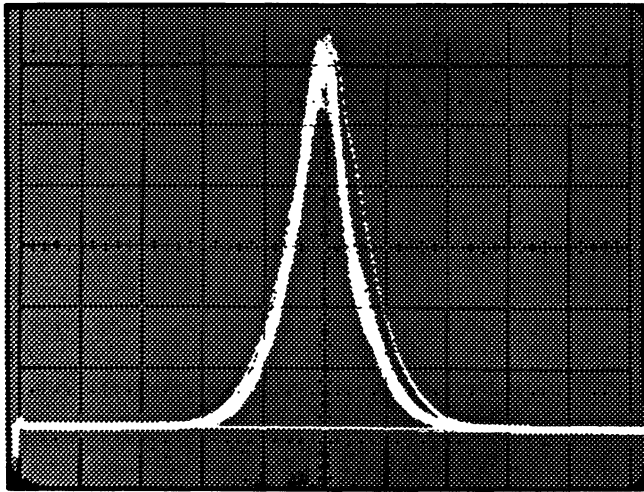
When making this measurement, one can either place the array at the true back focal plane of the lens, or in the plane which minimizes the width of the focal spot. The former arrangement measures the true total divergence of the beam, while the latter removes the contribution by the lowest order (cylindrical) divergence term. In general, the planes of minimum spot size will be different for vertical and horizontal scans of the focal spot, since the beam may be astigmatic. In the data to be presented here, we measure the total divergence. The true focal plane of the lens was determined by substituting a collimated beam from a He-Ne laser and finding its focus (minimum spot size as determined by the array), then translating the array (shortening the focus) by an amount computed from the known indices of refraction of fused silica at the two wavelengths.

Horizontal and vertical divergence profiles are shown in Figures 3(a) and 3(b). These are single traces taken during 200 Hz operation. The horizontal profile is Gaussian, with a  $1/e^2$  width of 2.44 mR (1.1 mR FWHM). The vertical profile has a  $1/e^2$  width of 3.8 mR (2.0 mR FWHM), and exhibits an asymmetry which is consistent with the intensity profile measurements. The right side, with the extended tail, corresponds to divergence upward above the optical axis.

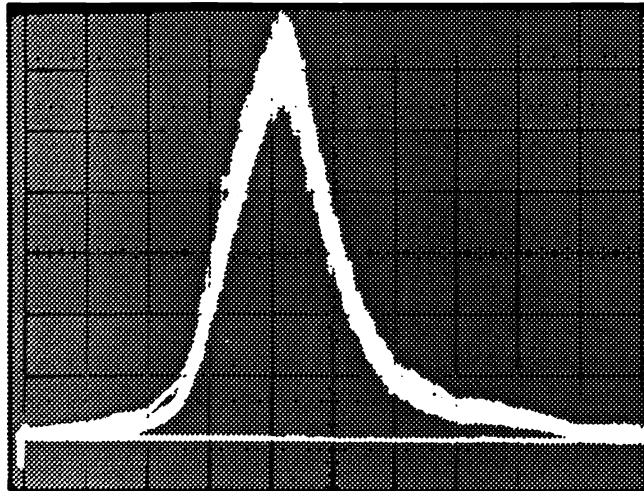
The transient response of the angular spectrum was explored by programming the laser to deliver a burst of 20 pulses at 200 Hz. Open-shutter photographs of the horizontal and vertical divergence profiles generated during this burst are shown in Figures 4 (a) and (b). The horizontal profile undergoes a narrowing and slight shift to the left between the first and subsequent pulses. The first pulse is somewhat wider than the rest, at 2.7 mR  $1/e^2$  (1.3 mR FWHM), and with a center shifted 0.1 mR to the right in Figure 4 (a). This transient beam-steering behavior is probably caused by the rapid buildup of horizontal thermal gradients in the laser discharge chamber, parallel to the laser gas flow. No similar shifting is seen for the vertical divergence during burst mode operation Figure 4(b).

### 4. POLARIZATION CHARACTERISTICS

The approximate polarization state of the laser was



4(a)



4(b)

Figure 4 (a) (b). Horizontal (a) and vertical (b) divergence profiles, showing transient mode behavior. Burst of 20 pulses at 200 Hz. Horizontal scale 1 mR/div.

first assessed using a stacked-plate polarizer mounted in a 360° rotary holder. The polarizer consisted of 8 fused silica plates inclined 65° to the optical axis, which produced a 55 to 1, p-polarization to s-polarization transmission ratio. The beam was passed through the polarizer and monitored by a photodiode. After rotating the polarizer about the optical axis and finding the transmission minimum, the beam was found to be polarized to within  $\pm 0.5^\circ$  of horizontal.

Next, two wedged, uncoated, fused silica substrates were arranged to give two successive Brewster-angle reflections in a horizontal plane, thereby selectively reflecting the vertical polarization component. Given a

layout accuracy of  $\pm 1^\circ$  in the angles of incidence, the extinction of the primary horizontal polarization component should be greater than  $1.8 \times 10^6$ . After correcting for the s-polarization reflection coefficient of the Brewster plates, the energy in the vertical polarization component of the beam was measured to be 0.468 mJ, or 3.12%, out of a total beam energy of 15 mJ. The polarization ratio, defined as  $(H-V)/(H+V)$ , was 93.8%. There was no change observed in the polarization ratio as the laser repetition rate was changed from 1 Hz to 200 Hz.

The intensity profile of the vertically polarized beam component exiting the Brewster plates was measured as before with a 1024 element photodiode array. The on-centerline vertical and horizontal profiles, shown in Figures 5 (a) and (b), are very similar to the full-beam profiles. The FWHM width and height are 3.9 and 18 mm, respectively.

## 5. SPECTRAL CHARACTERISTICS

### 5.1 Instrumentation.

Three different instruments were used to explore the spectral characteristics of the beam. The first was a Instruments SA THR1500 spectrometer. When used in double-pass configuration with a 3600 groove/mm grating, this 1.5 m instrument has a specified resolution of 0.8 pm at 248 nm. However, calibration scans of an iron hollow-cathode lamp indicated a practical resolution closer to 1.4 pm. The THR1500 spectrometer proved useful for taking general-purpose scans at moderately high resolution. It was not suitable for the highest resolution scans due to a comparatively coarse scanning step size (.3 pm), and poor thermal stability.

The second instrument, built in our laboratory, was a 1 m spectrometer using a grating at high angle of incidence. This is a specialized instrument suitable for taking very high resolution scans within a relatively narrow band: the theoretical resolving power is  $1.18 \times 10^6$  at 248 nm, giving a spectral slit width of 0.21 pm. The scanning step size is 0.016 pm/step, fine enough to generate a smooth, continuous spectrum. The major drawback of this instrument compared with the THR1500 spectrometer is its low throughput.

A Hamamatsu R292 photomultiplier tube (PMT) was used as the detector for both spectrometers. Care was taken to attenuate the UV signal from the laser to a level which maintained linear PMT response. Linearity tests of the tube indicated that no more than ap-

proximately 100 photoelectrons should be allowed to be emitted from the photocathode during each 15 ns pulse of the laser. At higher intensities, space-charge effects within the dynode chain start to reduce the electronic gain, leading to tube saturation.

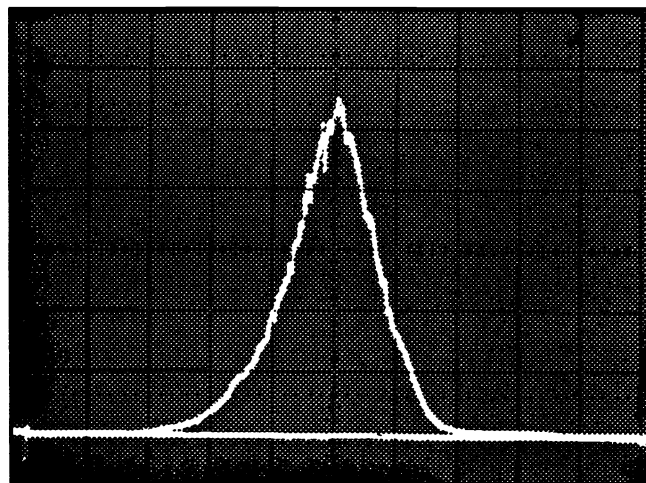
The third instrument used was the diagnostic etalon located within the wavelength stabilization module in the laser. This etalon has a free spectral range of 20 pm and a finesse of 30, giving a theoretical resolution of 0.67 pm. No direct measurement confirming the manufacturer's specifications was made. A 1024 element photodiode array forms the detector for this etalon. Unlike the spectrometers, which must scan the spectral profile and therefore collect spectral data over many thousands of shots of the laser, the etalon can provide a spectrum in one pulse. Its major drawbacks are its lack of sensitivity (the photodiode array is not sensitive enough to allow the use of spectral calibration lamps), and its inability to provide the precise shape of the laser spectrum

### 5.2 High Resolution Spectrum.

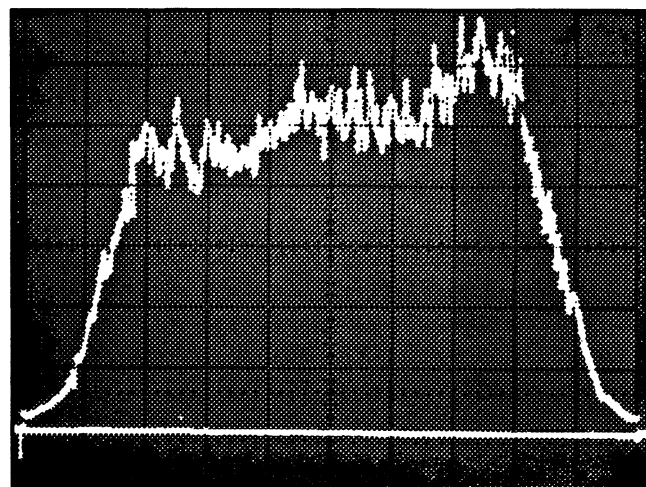
The spectrum of the full beam is shown in Figure 6, as taken by the high-resolution spectrometer. As with all spectral data to be presented here, the laser was operating at 200 Hz, 3 W output during the scan, and the beam was sent through a diffuser prior to introduction into the spectrometer to insure that all parts of the beam contribute equally to the spectrum. The spectrum has a decidedly Lorentzian shape, with a (non-deconvolved) bandwidth of 2.35 pm FWHM. A slight asymmetry can be seen.

Also included in Figure 6 are the theoretical spectrometer slit function, and the deconvolved spectrum. The spectrometer slit function is of the form  $\text{sinc}^2(x)$ , with a FWHM of 0.21 pm. Deconvolution was performed using fast-Fourier transforms of the data in the standard way (Ref. 2), which yielded a spectral width of 2.27 pm. By using the 'best case' performance of the spectrometer, the deconvolved spectrum represents an upper bound on the true width of the laser spectrum. As can be seen in Figure 6 the broadening effects of the spectrometer are small, amounting to only .08 pm. Integration of the deconvolved spectrum indicates that 95% of the spectral energy lies within a 7.1 pm band.

The spectrum from the diagnostic etalon and the theoretical etalon bandpass function are presented in Figure 7. The etalon trace represents three shots (taken at 200 Hz) which were digitized, averaged and smoothed by a binomial smoothing algorithm in order



5(a)



5(b)

Figure 5 (a) (b). Horizontal (a) and vertical (b) intensity profiles of the minor vertical polarization component, which makes up about 3% of the beam energy. Horizontal scale 2.5 mm/div.

to reduce noise which would interfere with the deconvolution process. The deconvolved etalon spectrum is also presented in Figure 7. The bandwidth is slightly narrower, 2.15 pm FWHM, than that measured by the high resolution spectrometer, but still in good agreement.

A brief discussion is in order concerning the convolution process and the rules-of-thumb it generates for estimating the true bandwidth from data which includes broadening effects of the measuring instrument. The functional shape of the two convolving functions, especially the behavior in the tails of the spectrum, is critically important in determining how much broadening

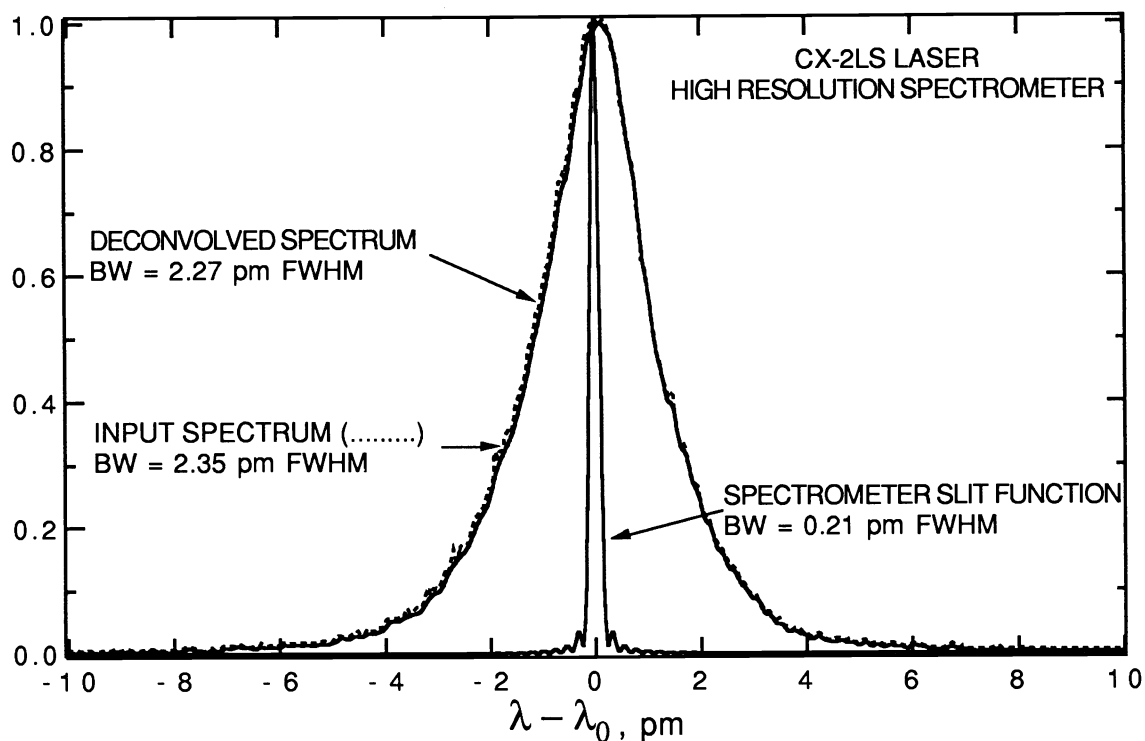


Figure 6. Laser spectrum as taken by the high resolution spectrometer (dashed curve). The deconvolved spectrum (solid curve) is also shown, along with the theoretical spectrometer slit function. The bandwidth is found to be 2.27 pm FWHM, with 95% of the energy within a 7.1 pm band.

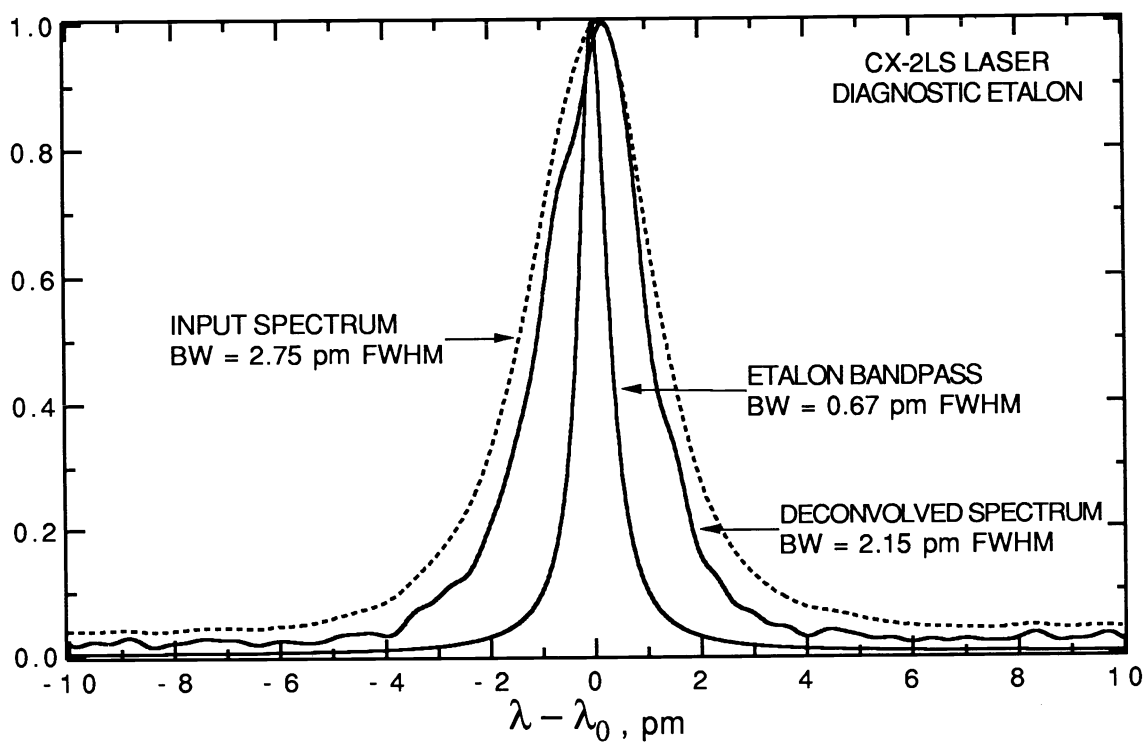


Figure 7. Laser spectrum as taken by the diagnostic etalon (dashed curve). The deconvolved spectrum (solid curve) is also shown, as well as the theoretical etalon bandpass function (FSR = 20 pm, finesse = 30).

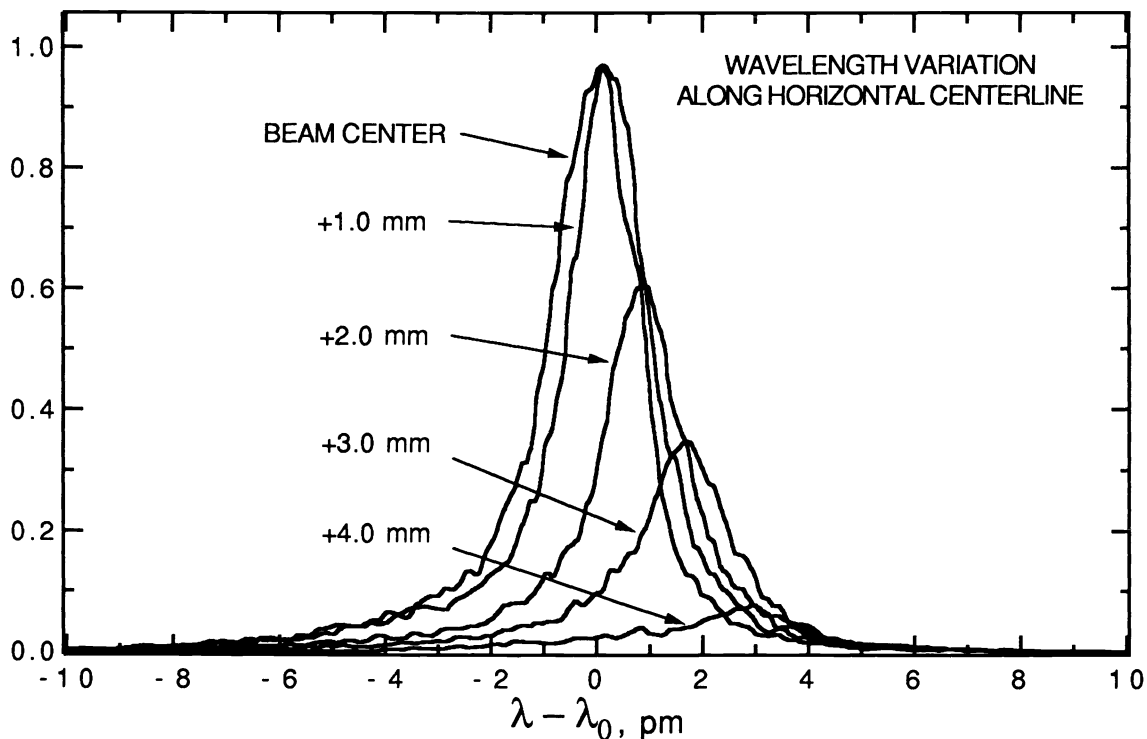


Figure 8. Variation in the spectral content of the beam as a vertical slit mask selects out portions of the beam, scanning horizontally from beam center to the right. The variation in height of the spectra reflects the horizontal intensity profile.

takes place. Two Gaussians, for instance, convolve to another Gaussian whose FWHM width  $\Gamma$  is the quadratic sum of the convolving widths:  $\Gamma^2 = \Gamma_1^2 + \Gamma_2^2$ . Two Lorentzians, on the other hand, convolve to another Lorentzian with a width equal to the simple sum:  $\Gamma = \Gamma_1 + \Gamma_2$ . Combinations of these and other functions yield deconvolution rules usually in between these two cases. It can be easily shown that the etalon band-pass function closely approximates a Lorentzian shape. Since the laser spectrum is also closely Lorentzian, the bandwidth as determined by the etalon can be justifiably corrected by simply subtracting the etalon resolution (see Figure 7). The high resolution spectrometer is an interesting case because its slit function,  $\text{sinc}^2$ , looks roughly like a  $\sin^2$  function with a Lorentzian envelope. When convolved with a Lorentzian, the deconvolution rule takes on the modified form  $\Gamma = \Gamma_1 + k \Gamma_2$ , where  $k \approx .3$  to  $.4$  over a remarkable range:  $3 < \Gamma_1 / \Gamma_2 < 25$ . A mid-range value of  $k = .35$  gives bandwidth corrections to greater accuracy than the measurement of the convolved data.

### 5.3 Wavelength Variation.

The THR1500 spectrometer was next used to study the variation of the spectral content of the beam as a

function of position within the beam. A  $100 \mu\text{m} \times 2 \text{cm}$  slit mask, oriented either vertically or horizontally, was used to select a thin slice of the beam at various locations. After passing through a diffuser, the light was introduced into one split end of a bifurcated fiber-optic bundle. The light from an iron hollow-cathode lamp was introduced into the other split end as a spectral reference. Light from both sources exited the far (non-split) end of the bundle spatially intermixed, and was introduced into the spectrometer. Spatial inter-mixing of the two radiation sources insures a nearly identical input geometry to the spectrometer, giving consistent spectral registration between the laser radiation and the reference lamp.

Spectral scans were taken of the light passing through the slit mask for several positions within the beam, and for vertical and horizontal orientation of the slit mask. The iron reference line chosen was a strong line at 248.3271 nm. During the scan, the laser was tuned to the *same wavelength as the reference line*. Since the laser produces short pulses of light at precisely predictable times, separation of the CW reference lamp from the laser signal was straightforward using time gating techniques. This arrangement eliminates to a large degree possible calibration errors caused by im-

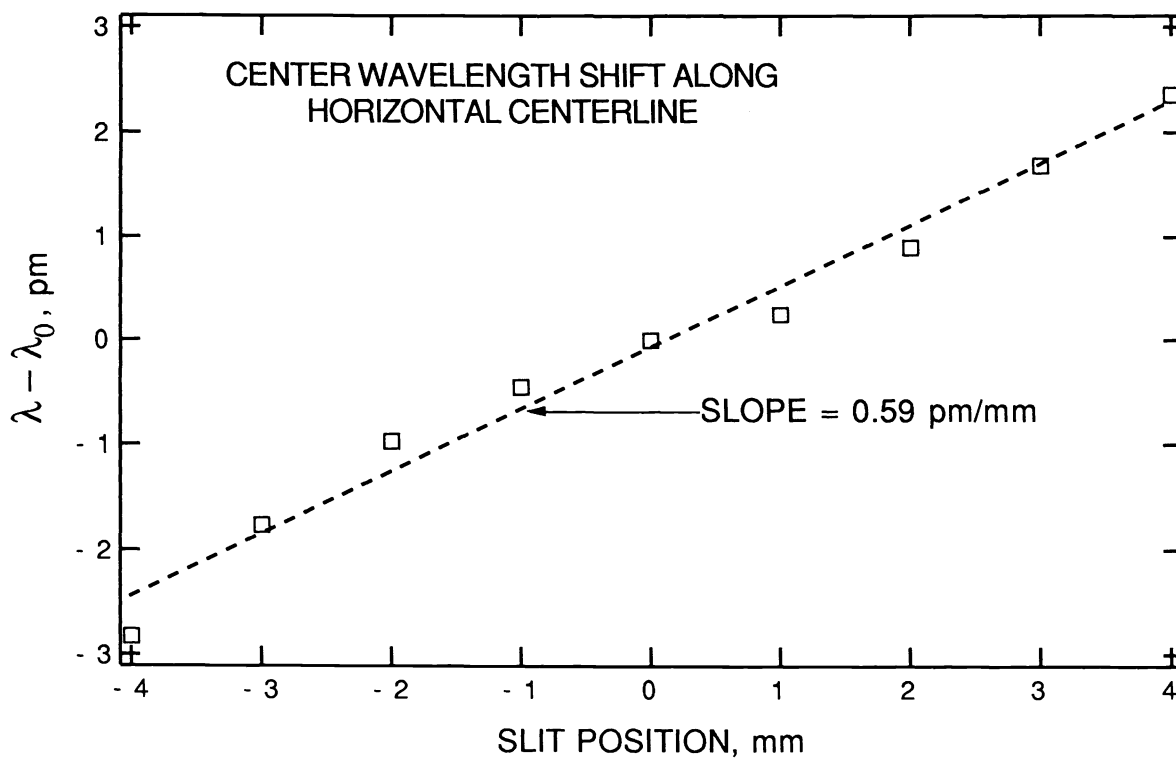


Figure 9. Plot of the systematic shift in wavelength as a slit mask scans from one side of the beam to the other. A least-squares linear fit (dashed line) gives a slope of 0.59 pm/div.

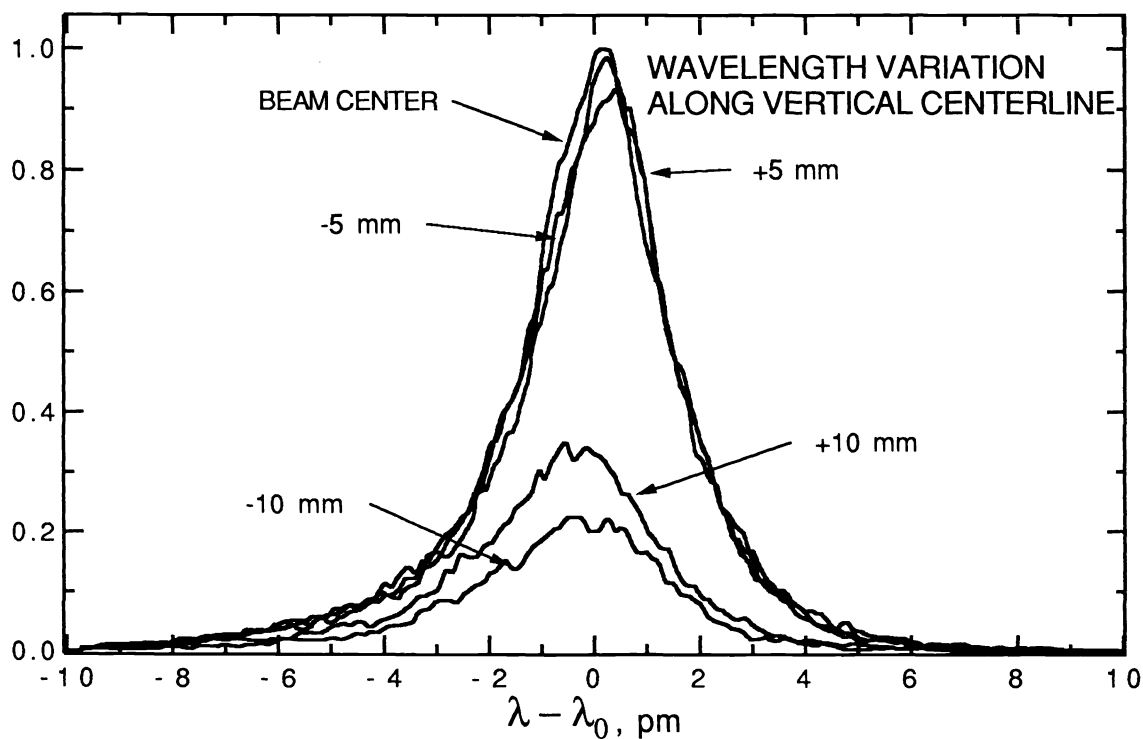


Figure 10. Variation in the spectral content of the beam as a horizontal slit scans the beam vertically. No significant wavelength variation is seen along the vertical axis.

perfections in the mechanical sine-drive in the spectrometer. A two-channel chart recorder simultaneously recorded the laser and reference spectra. After all scans were taken, the data was digitized using the trace of the iron reference line to overlay the spectra.

The resulting data are plotted in Figures 8, 9, and 10. Figure 8 shows the systematic shift in the center wavelength (wavelength 'chirping') as a vertically oriented slit is scanned horizontally to the right from the centerline. The relative amplitudes of the scans reflect the horizontal intensity profile of the beam. The shift in the central wavelength with horizontal position is a consequence of using a grating in the laser resonator. Figure 9 shows how the wavelength shifts as a function of slit mask position along the entire horizontal cross-section. A least-squares linear fit to the data shows a .59 pm/mm slope.

Scanning the beam along the vertical axis with a horizontal slit mask yields the data of Figure 10. Since the line-narrowing optics generate no dispersion in the vertical direction, no wavelength variation was observed.

#### 5.4 Broadband Background Scan.

The laser spectrum was examined for the possible presence of any low-level, broadband background radiation. The cumulative effects of such a background can cause a reduction in resolution at the wafer plane, since the images produced by these out-of-band wavelengths will be out of focus. Within the laser, broad-band backgrounds can rise to significant levels if care is not taken to suppress on-axis stray reflections within the optical resonator.

Two scans of the beam were taken with the THR1500 spectrometer, the first at normal intensity, generating a full-scale spectral scan, and the second with an optical gain ten times higher (i.e. attenuators were removed). The laser was tuned to the iron reference line at 248.327 nm, and the wavelength range from 248.227–248.427 nm scanned. As before, the light from an iron spectral calibration lamp was folded in and recorded along with the laser. The overlaid scans are presented in Figure 11. The tails of the spectrum are down to the 0.1% level within  $\pm 15$  pm of line center, and they dropped below our limits of detection within  $\pm 20$  pm.

#### 5.5 Spectral Shape Versus Polarization.

To complete the investigation of the polarization characteristics of the beam, the spectra of both the vertical and horizontal polarization components were taken by the THR1500 spectrometer, along with the usual simultaneous scan of the iron reference line. Brewster plates selected out the vertical component as detailed above. Both spectra are shown in Figure 12, normalized to the same vertical scale. No difference is seen between the two spectra, either in shape, width, or center wavelength.

### 6. COHERENCE PROPERTIES

In order to minimize the interference effects of speckle, DUV lithography would ideally like to employ an 'incoherent' laser, one whose coherence properties are more like a narrow-band, incoherent lamp than like a laser. Although various techniques are currently in use to 'scramble' the beam in order to average out the speckle (and improve uniformity), the shorter the coherence length of the laser the better. Early DUV lithography work used injection-locked laser designs which proved to be too spatially coherent. Subsequent development of efficient line-narrowing techniques have produced the current generation of narrow-band, high-order spatial mode power oscillators. The coherence properties of the beam are examined in this final section.

We adopt here the nomenclature used by Born and Wolf (Ref. 3) for describing the coherence properties of (stationary) optical fields. When two light waves interfere, and for our purposes here we mean two rays selected from different positions within a single beam, the resultant pattern is given by

$$I_T = I_1 + I_2 + 2 \sqrt{I_1 I_2} |\gamma_{12}(x_1, x_2, \tau)| \cos(\delta(x_1, x_2, \tau))$$

where  $I_1, I_2$  = the intensities at positions  $x_1, x_2$  and at times  $t_1, t_2$ . Since most physical processes are stationary, the time dependency reduces to the difference  $\tau = t_1 - t_2$ . The cosine term generates the familiar fringe pattern formed by the interference of the coherent components of the beam, with its argument  $\delta(x_1, x_2, \tau)$  containing the geometrical details of how the beams are allowed to interfere. The coefficient  $|\gamma_{12}(x_1, x_2, \tau)|$  is of interest here, since it determines the amplitude of the fringe pattern.  $\gamma_{12}(x_1, x_2, \tau)$  is called the (normalized) complex degree of coherence. Physically, it repre-

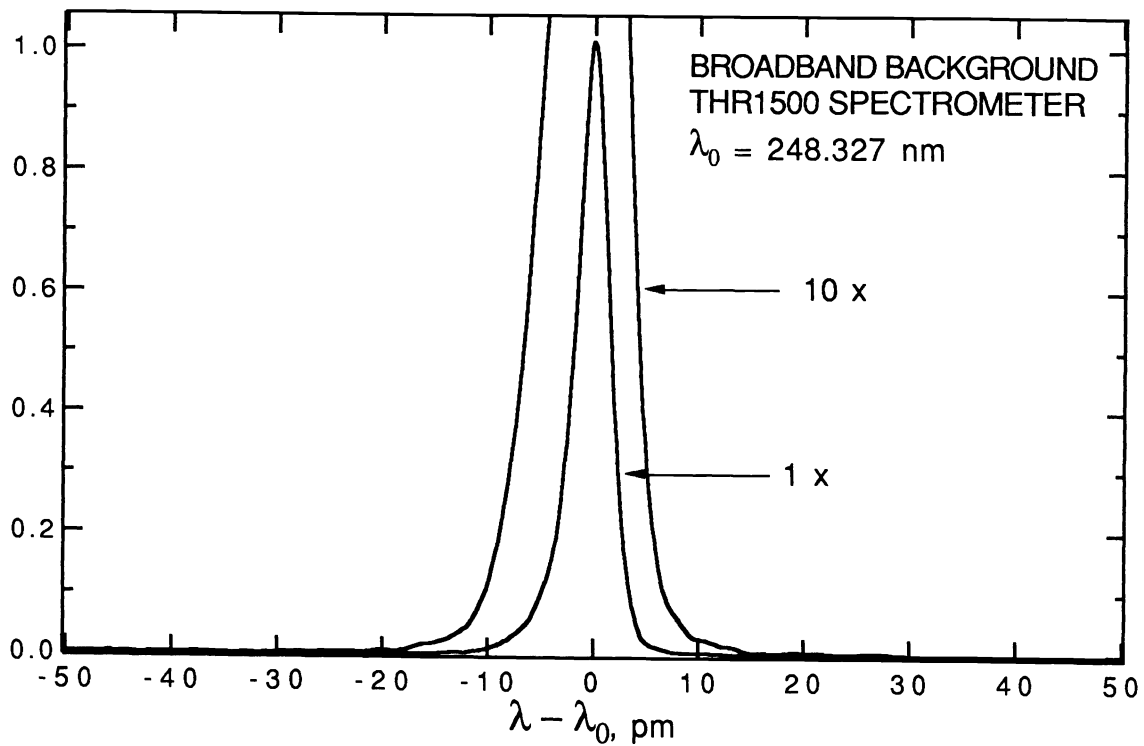


Figure 11. Broadband background radiation scan. The 10x curve was taken by boosting the optical gain (i.e. attenuators were removed). The tails of the spectrum are down to 0.1% within  $\pm 15 \text{ pm}$  of line center.

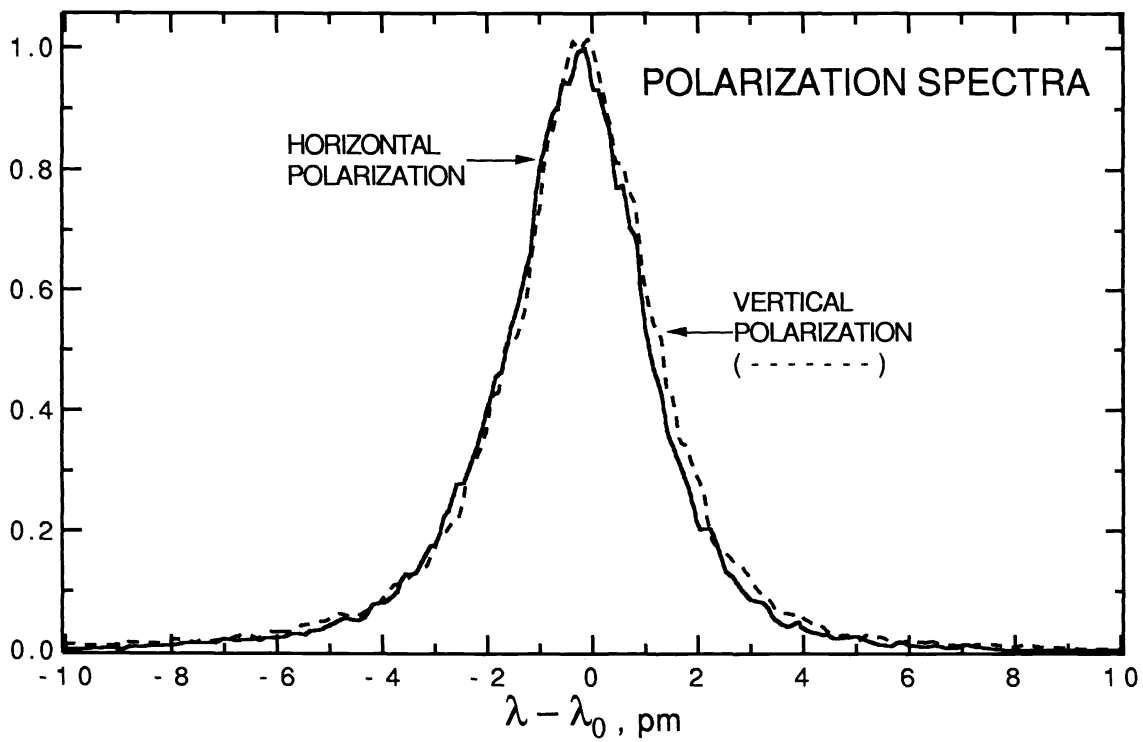


Figure 12. Comparison of the spectra of the horizontal and vertical polarization components.

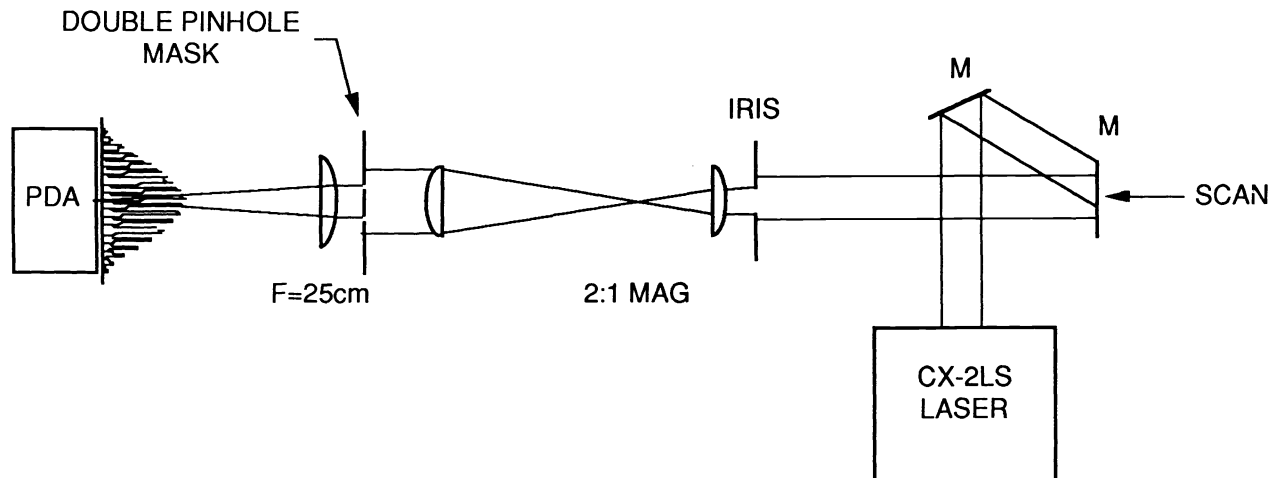


Figure 13. Optical arrangement used to measure the spatial coherence function by the double-pinhole interference method.

sents the ratio of the coherent intensity to total intensity, taking on values between 0 (for incoherent fields) and 1 (for coherent fields).

Two special cases of  $\gamma_{12}(x_1, x_2, \tau)$  are commonly used to describe the coherence properties of a beam. When the two interfering rays originate at different points  $x_1, x_2$ , but pass through these points at essentially the same time, so that  $\tau = 0$ , the magnitude of the complex coherence has the form  $|\gamma_{12}(x_1, x_2, 0)| = |\mu_{12}|$  and is called the 'spatial coherence' function.  $|\mu_{12}|$  describes the rate at which the fields for different parts of the beam 'decorrelate' as the separation between them increases. As it's commonly used,  $|\mu_{12}|$  is thought of as 'quasi-stationary', depending mainly on the separation between the points  $x_2 - x_1$ , but perhaps also weakly dependent on the region within the beam where the points are located.

The second special case involves interference between two interfering rays originating at the same point ( $x_2 = x_1$ ) but which pass through this point at different times separated by  $\tau$ . In this case,  $|\gamma_{11}(x_1, x_1, \tau)| = |\gamma(\tau)|$ , where  $|\gamma(\tau)|$  is the 'temporal coherence' function, and is essentially the longitudinal equivalent of the spatial coherence. The temporal coherence time  $\tau$

may be converted to a longitudinal coherence length  $z$  via  $z = c\tau$ .

### 6.1 Spatial Coherence.

Measurement of the spatial coherence properties of the CX-2LS was performed using the 'double pinhole interference' technique (Ref. 5). In this arrangement, a mask with two small, finely spaced pinholes is illuminated by the beam and the Fraunhofer interference pattern measured using a 1024 element photodiode array. The spatial coherence function  $|\mu_{12}|$  for a given hole separation is equal to the fringe visibility at the detector,  $V = (I_{\max} - I_{\min}) / (I_{\max} + I_{\min})$ . By taking measurements using a collection of masks with different pinhole separations, the spatial coherence function can be mapped out. Horizontal and vertical pinhole separations are used to measure horizontal and vertical spatial coherence, respectively.

The excimer laser itself was used to drill 25  $\mu\text{m}$  holes in 50m thick mylar. Masks with pinhole separations of 50, 100, 150, 200, 300, 400, 500, and 600  $\mu\text{m}$  were produced. The masks were used in the optical arrangement shown in Figure 13. After reflecting off turning mirrors, which permits the beam to be scanned

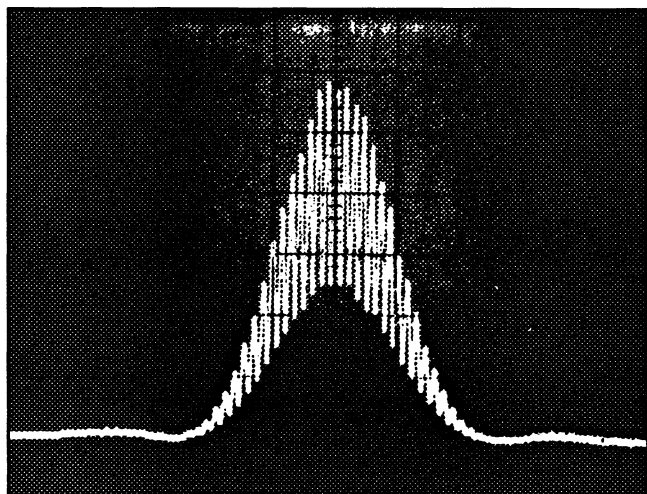


Figure 14. Typical double-pinhole interference pattern generated by the optical setup of Figure 13. 300  $\mu\text{m}$  horizontal pinhole spacing.

across the input aperture, the beam was magnified 2X by a simple telescope before illuminating the mask. The resulting interference pattern was detected in the Fourier plane of a 25 cm lens by a photodiode array. A typical interference pattern is shown in Figure 14.

The horizontal and vertical spatial coherence functions, measured at beam center, are shown in Figure 15. Note that in Figure 15 and the discussion below we use coherence lengths characteristic of the beam as it exits the laser, before the 2x beam expander. The vertical coherence length  $L_V$ , defined as the spacing at which the coherence function falls to 0.5, is only 60  $\mu\text{m}$ . The horizontal coherence length  $L_H$  is approximately twice as long, at 126  $\mu\text{m}$ . While the fringe visibility was consistent for most measurements of  $|\mu_{12}|$ , for  $|\mu_{12}| < 0.2$  the fringe visibility fluctuated quite a bit from pulse to pulse, from nearly zero to the values recorded. The data presented, therefore, represents an upper bound on the coherence function in this region.

Since the coherence lengths are inversely related to the number of spatial modes propagating within the cavity, the unequal coherence lengths imply fewer spatial modes in the horizontal direction. This is clearly reflected in the divergence data, where the ratio of the horizontal to vertical divergence is in the same 1:2 inverse ratio. Ichihara, et.al. (Ref 6) have found that the divergence and spatial coherence length are related by  $\Theta_d L = 2 \lambda$ , where  $\Theta_d$  is the full angle of divergence and  $L$  is the coherence length. In that work, measurements which confirmed this relation were made on an

excimer laser spectrally narrowed by etalons. We find that this relation also holds for the CX-2LS, which is spectrally narrowed by a grating, provided  $1/e^2$  values for both the divergence and spatial coherence length are used. For example, using 2.44 and 3.8 mR for the horizontal and vertical divergences, the above relation predicts 204 and 131  $\mu\text{m}$  for  $L_H$  and  $L_V$  ( $1/e^2$ ), respectively, in good agreement with Figure 15.

An assumption commonly made when describing beam coherence is that the coherence properties are the same for all parts of the beam. We tested this assumption by measuring the (local) spatial coherence lengths  $L_V$  and  $L_H$  for various positions along the beam centerlines. The combined results are plotted in Figure 16. The coherence length was found to be remarkably consistent along these centerlines.

## 6.2 Temporal Coherence.

The temporal coherence function  $|\gamma(\tau)|$  was measured using a Michelson interferometer, shown in Figure 17. One leg was adjustable in length by translating one of the mirrors. The central beam splitter was an uncoated, wedged fused silica plate. To avoid upsetting the normal polarization ratio, the interferometer was arranged with the beam splitter at approximately  $15^\circ$  to the input beam instead of the usual  $45^\circ$ . The interferometer was aligned so that the two output beams converged at a slight angle to each other in the horizontal plane, producing vertical fringes on the photodiode array. When the two legs of the interferometer were matched in length ( $\tau = 0$ ), and the output beams spatially overlapped to well within the spatial coherence lengths ( $x_2 = x_1$ ), strong fringes with 96% visibility were obtained.

Measurement of the temporal coherence function proceeded by progressively lengthening the adjustable leg of the interferometer and recording the resultant fringe visibility. After each increment, the alignment was adjusted to achieve maximum fringe visibility. The resulting temporal coherence function is shown in Figure 18. The temporal coherence length  $L_T$ , the length for which the coherence function drops to 0.5, was found to be 33.3 mm.

The temporal coherence length is order-of-magnitude related to the spectral bandwidth by (Ref. 4):

$$L_T \approx \lambda^2 / \Delta\lambda$$

A 33.3 mm coherence length implies a spectral bandwidth of 1.85 pm, in reasonable agreement with the

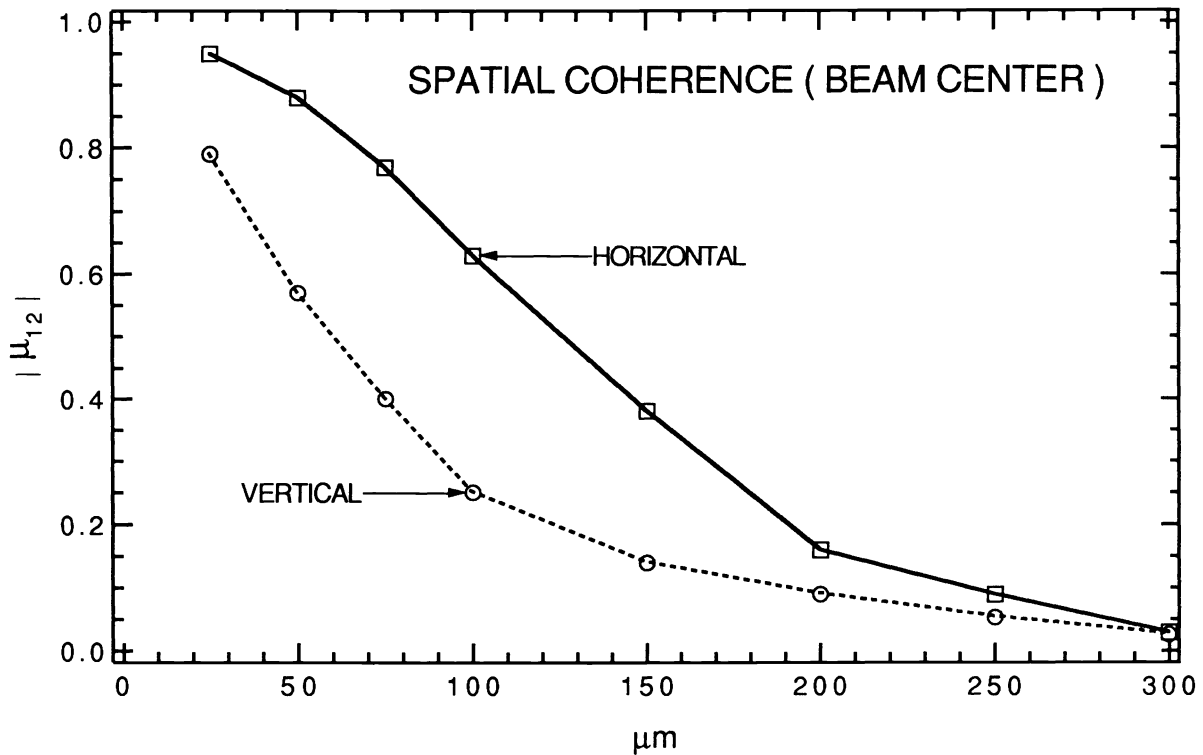


Figure 15. Vertical and horizontal spatial coherence function  $|\mu_{12}|$ , measured on beam center. The coherence lengths, where  $|\mu_{12}| = 0.5$ , are  $60 \mu\text{m}$  (vertical) and  $126 \mu\text{m}$  (horizontal).

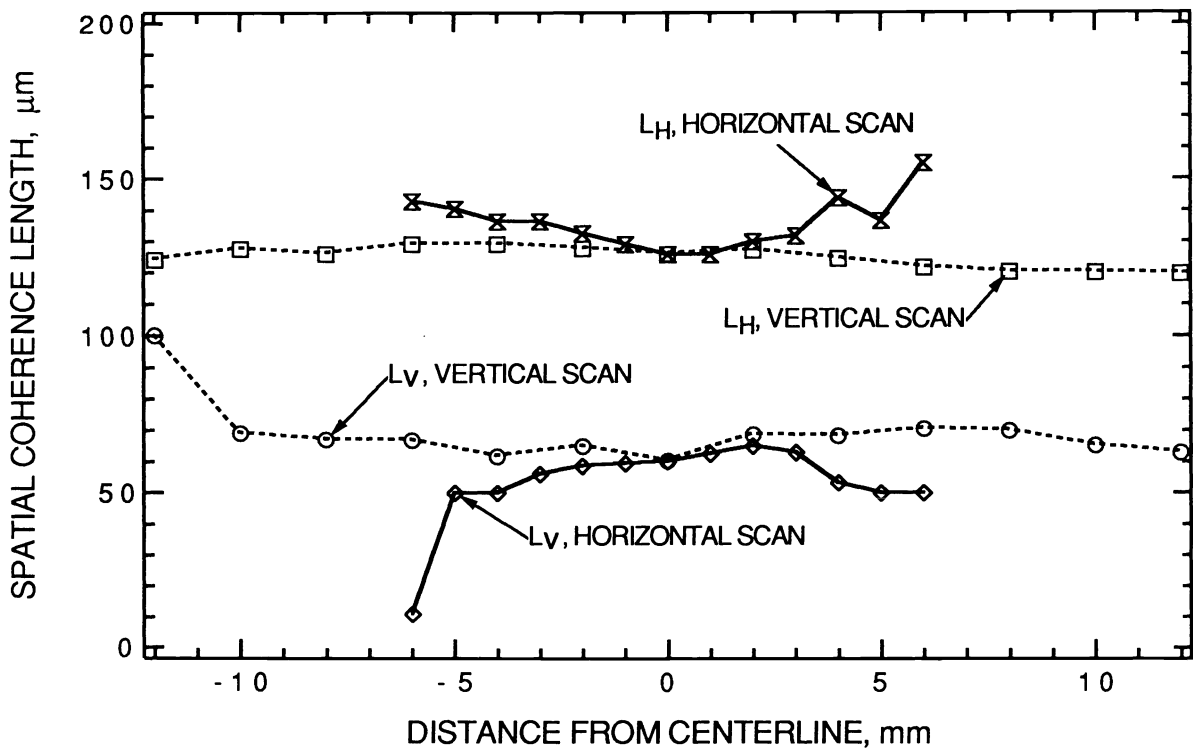


Figure 16. Variation of the vertical and horizontal spatial coherence lengths along the vertical and horizontal beam centerlines.

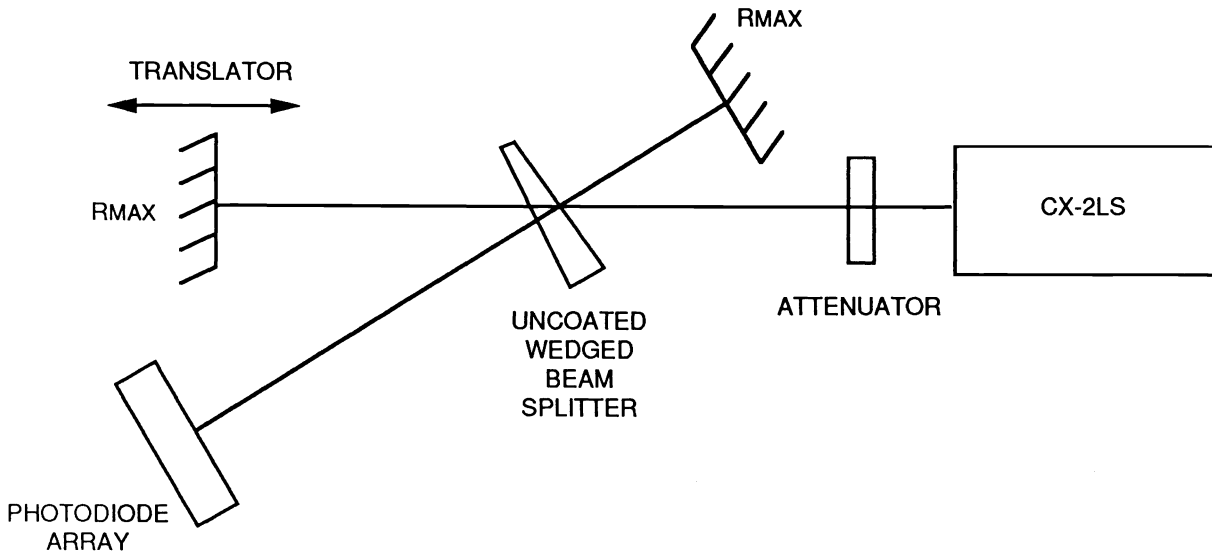


Figure 17. Michelson interferometer used to take temporal coherence data. The skewed shape of the arrangement avoids changes in the polarization state of the beam.

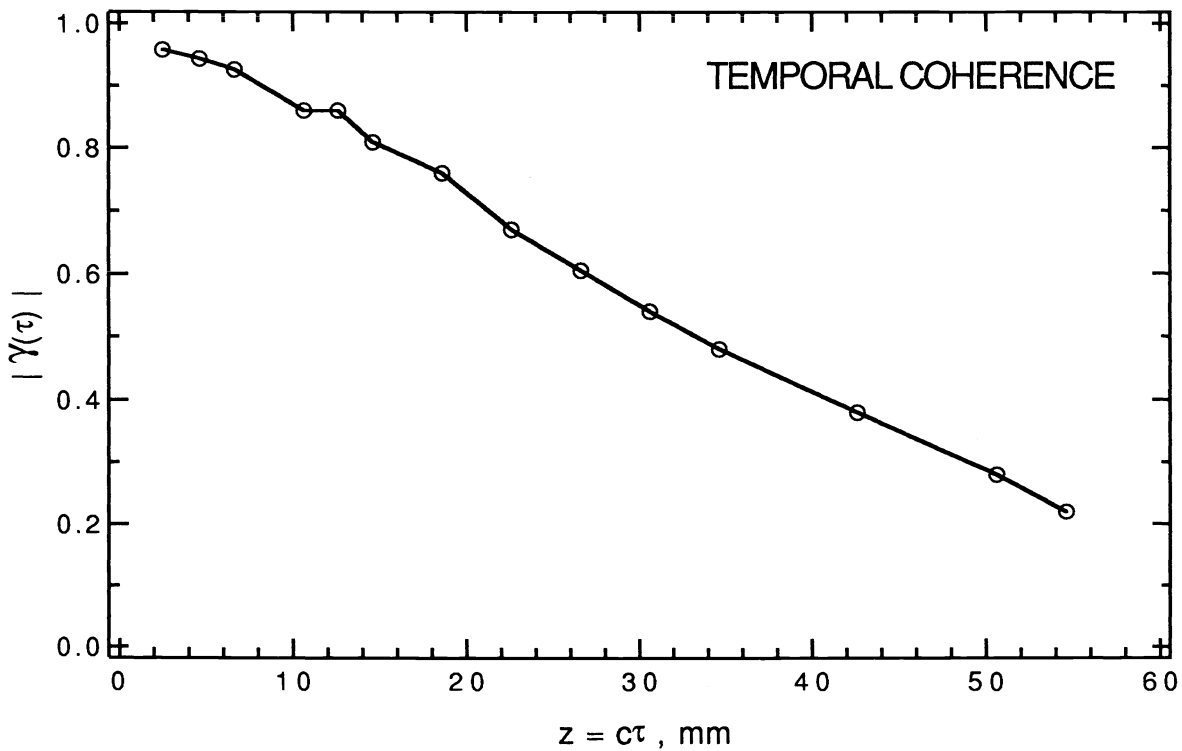


Figure 18. Temporal coherence function  $|\gamma(\tau)|$  as taken with the Michelson interferometer of Figure 17. The temporal coherence length is 33.3 mm.

2.25 pm measured previously using the high resolution spectrometer.

### 7. CONCLUSION

Work is continuing on refining both the technical specifications of the CX-2LS laser and the methods for their measurement. It should be noted that the data presented above represents a 'snapshot' of the optical performance of one production laser at a point approximately 10% of the way through its lifecycle. Variation in the optical characteristics of the beam as a function of gas life, and as the laser ages is currently under investigation.

### 8. ACKNOWLEDGEMENTS

The author would like to thank Chris Reiser, Uday Sengupta, and Robert Akins for their thoughtful critiques of the manuscript. Thanks also to Suzanne Brown and Greg Koppman-Gue for preparing the manuscript for publication.

### 9. REFERENCES

1. R.L.Sandstrom, et.al., 'Krypton Fluoride Excimer Laser for Microlithography', presented at the 1989 SPIE Symposium on Microlithography, paper 1088-43.
2. W. H. Press, et. al., *Numerical Recipes : The Art of Scientific Computing* , pg. 407 ff. (New York, N.Y.: Cambridge Press, 1986)
3. Max Born, and Emil Wolf , *Principles of Optics*, (6th Ed.), pg. 499 ff. (Elmsford,N.Y.: Pergamon Press, 1980)
4. Born and Wolf, *ibid*, pg. 319.
5. Born and Wolf, *ibid*, pg. 513 ff.
6. Y. Ichihara, et.al., Nikon Corp., 'Illumination System of an Excimer Laser Stepper', presented at the 1989 SPIE Symposium on Optical Microlithography and Metrology for Microcircuit Fabrication. Published in SPIE proceedings VOL. 1138 pg 137 - 143.